Investigating HBC 494's Wide-Angle Outflows

Austen C. Fourkas,[1,2]★
[1]National Radio Astronomy Observatory, Charlottesville VA
[2]University of Maryland College Park, College Park MD

25 August 2021

ABSTRACT

I present spectral analysis of HBC 494, a FUor type binary star system located in the constellation Orion. Specifically, I present ALMA observations of ^{12}CO, ^{13}CO, C^{18}O, and SO emission lines, all of which trace different regions of HBC 494. By using a combination of the ALMA 12 meter, ACA, and total power arrays, a field of view of $\sim$ 1600 arcseconds^2 was achieved and allowed for the detection of an upper cavity 15″ North of the central object. This cavity appears to be connected kinematically to the central object, implying a relationship to HBC 494's large-scale accretion mechanism.

Key words: HBC 494 (more to come)

1 INTRODUCTION

1.1 Star formation and Young Stellar Objects

The process of star-formation is initiated by the gravitational collapse of a slowly-rotating core comprised of molecular gas and dust. This collapsing core eventually forms a Young Stellar Object (YSO), at its center. Young stellar objects are a Class of celestial objects which serve as standards for the early star formation process. These objects are classified as class 0, I, II and III, with an object's Class value increasing as its age increases. Classification value is derived from a YSO's spectral energy diagram (SED), specifically the diagram's slope, also called spectral index, in the range of $2 - 25\mu m$ (Williams & Cieza 2011). SEDs for the four primary classes of YSOs can be seen in figure 1, and approximate numerical classification boundaries can be found in table 1. Because SEDs typically use logarithmic axes, the slope slope of the diagram is given as the following, in which F_λ is the flux density at a wavelength λ:

$$\alpha = \frac{d \log \lambda F_\lambda}{d \log \lambda}. \quad (1)$$

Classification is not always so straightforward, however. Spectral energy diagrams fail to account for spatial properties, and the inclination of a YSO can have a large impact on its SED, and thus its classification. At high inclinations ($i \gtrsim 60°$), Class II YSOs may be misclassified as Class I, and Class I YSOs may be misclassified as Class 0 (Williams & Cieza 2011). Complete classification can only be achieved with resolved images at multiple wavelengths, although this is difficult due to the physical environment surrounding many YSOs.

1.1.1 Class 0 objects

Class 0 YSOs are formed from a cloud of cold, dense gas and dust. Due to environmental turbulence and other external forces, the cloud eventually starts collapsing onto a point source and a protostar begins to form. As the core of the cloud collapses, conservation of energy and angular momentum take hold, which establishes an axis and direction of rotation for the system as well as a circumstellar disk. Infalling material from the stellar envelope causes the central protostellar core to increase in size, and thus in temperature, which leads to a noticeable shift in the object's spectral energy diagram. Due to their temperature, these objects cannot be detected by their spectral index, and other methods must be used instead.

Table 1. A breakdown of the SED slopes which define each YSO Class (interpreted from (Williams & Cieza 2011))

Class	Slope	Characteristics
0	Undetectable	Nearly zero near-IR or optical emission
I	$\alpha > 0.3$	Usually obscured optically
FS	$0.3 > \alpha > -0.3$	Stage in between Class I & II
II	$-0.3 > \alpha > -1.6$	Noticeable accretion and Hα emission
III	$\alpha < -1.6$	Non-accreting disk and high chance of debris

1.1.2 Class I objects

Class I objects are characterized by a spectral index greater than 0.3. During this phase, accretion onto the central object becomes extremely prevalent. The protostar accretes matter from the inner regions of the circumstellar disk, which is itself supplied matter by the outer regions of the disk. As more and more matter infalls from the stellar envelope, to the outer disk, the inner disk, and finally the central protostar, outflows can form on opposite poles of the protostar due to the conservation of angular momentum (Fig. 2). Outflows of this nature may also be present in Class 0 objects, but due to their highly embedded nature, are extremely difficult to observe. The bipolar nature of these outflows can aid in determining both the axis of rotation of the system, as well as its Class, as they can persist well beyond the Class I phase (Principe et al. 2017). Highly collimated outflows are indicative of younger (Class 0-I) systems, while wider outflows are often present in older (late Class I-II) systems (Arce et al.

★ E-mail: afourkas@umd.edu

Figure 1. This diagram displays SEDs of Class 0 - III YSOs, as well as illustrations of their approximate structure (André 2002).

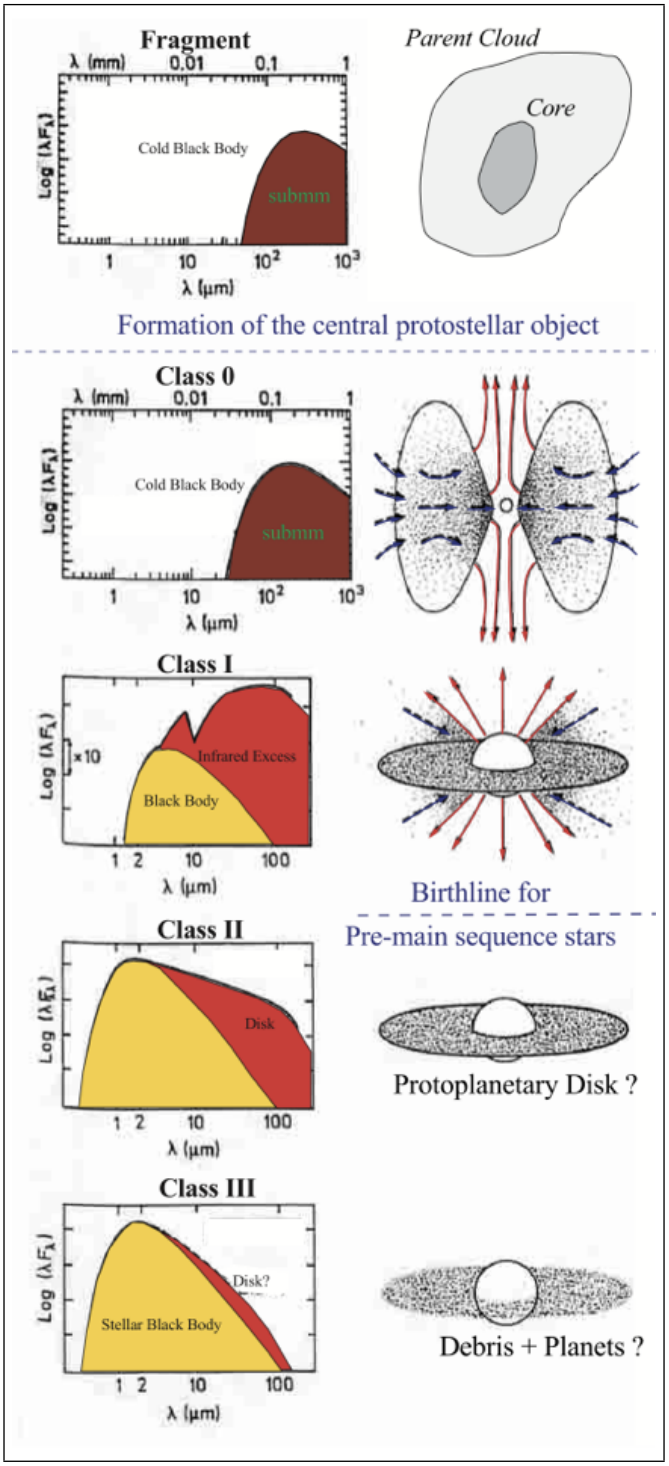

Figure 2. An illustration of a the general structure of a Class I YSO [not to scale]

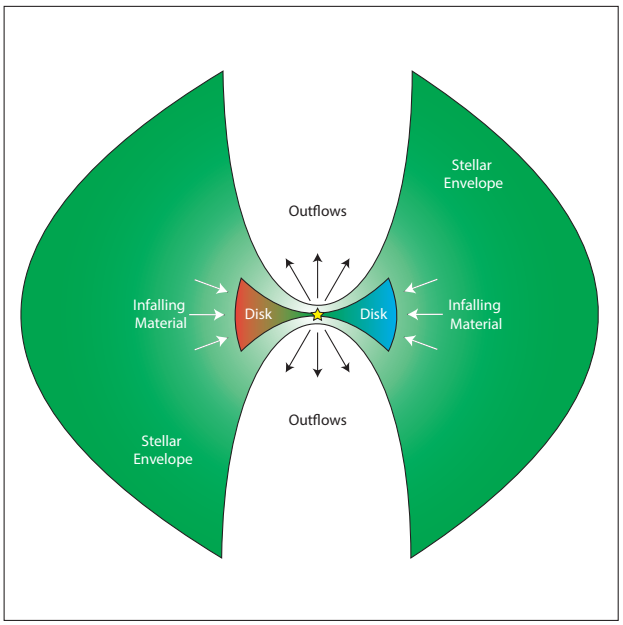

2010). The protostellar envelope can only feed the outer disk for so long before dissipating, meaning that prevalent envelope emission is indicative of a Class 0/1 YSO. In accordance with the complete dissipation of the protostellar envelope and relatively high accretion rates, the end of the Class I phase is marked by the end of the central protostar's formation, which induces a significant change in the YSO's SED (Williams & Cieza 2011).

1.1.3 Class II & III objects

The Class II and Class III stages mark the final steps in a YSO's evolution towards the main sequence. By the beginning of the Class II phase, the outer disk is no longer fed by the stellar envelope, which leaves dust settling and grain growth, accretion, and photoevaporation as the primary influences on the disk's mass, radius, and composition (Williams & Cieza 2011). Up to the beginning of the Class II phase, accretion from the disk dominates the central star's photoevaporation rate, allowing for the outer disk to act as a reservoir for the inner disk. The inner disk cannot maintain this accretion rate on long timescales, however, and eventually equilibrates with the photoevaporation rate. At this point, the outer disk can no longer resupply the inner disk, and a gap forms between the two (Williams & Cieza 2011). This gap enables X-ray and far-UV radiation to quickly erode the inner edge of the outer disk, leaving only a debris disk behind (Fig. 3-C) (Williams & Cieza 2011). The formation of the debris disk marks the transition from Class II to Class III, and allows for the formation of large planetecimals and eventually fully-fledged planets (Fig. 3-D).

1.2 FUors

Class I YSOs exhibit a unique discrepancy between their masses, luminosities, and theoretical accretion rates. Known as the 'luminosity problem', this phenomenon highlights the fact that mass and luminosity predictions based on constant accretion models do not align with measured values from various YSOs (Audard et al. 2014). Due to these inconsistencies, models which feature instances, or bursts, of extreme accretion have become popular in solving this problem. FU Ori, or FUor, type objects are possible solutions to the luminosity problem, and exist as a short-lived phase within the Class 0, I, or II phase of a YSO. A typical FUor outburst event is characterized by notable changes in accretion rate, magnitude, and spectral energy diagram. Many models exist which could explain these outbursts, and include, but are not limited to: instability introduced by planets, a combination of gravitational and magnetorotational instability, disk

Figure 3. An illustration of the disk evolution of a Class I/II YSO [not to scale]

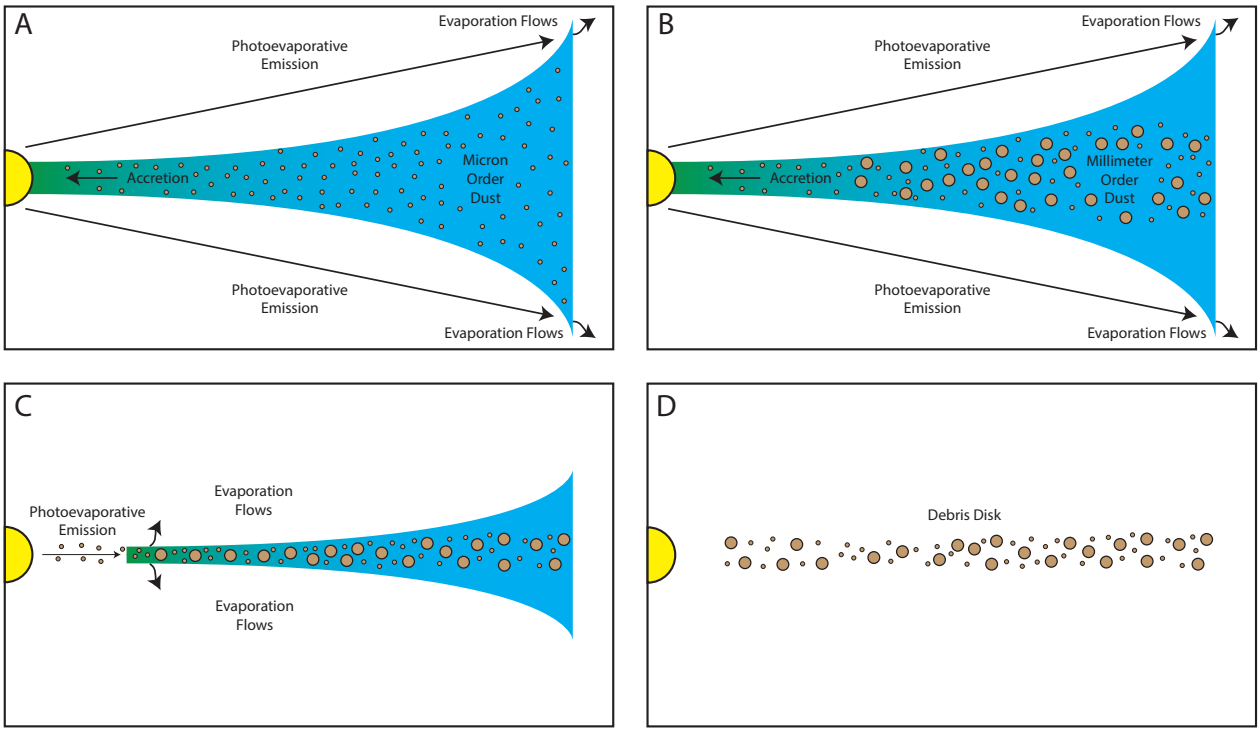

fragmentation, and possible external triggers (Audard et al. 2014). Magnitude changes of order $\Delta M = 5$ have been noted by multiple observation campaigns, and accretion rate changes on the order of $\sim 10^{-7} \rightarrow 10^{-4}\,M_{\odot}\,yr^{-1}$ have also been observed multiple times (Audard et al. 2014). FUors can also exhibit both stochastic and semi-periodic short-timescale variability (Audard et al. 2014). This variability has been attributed to many sources, but small accretion changes, plasma condensations, and localized disk heterogeneities are the most popular explanations (Audard et al. 2014; Kenyon et al. 2000; Siwak et al. 2013). FUors typically share multiple spectral features with F-G supergiant stars, as well as certain near-IR water vapor bands with K-M supergiants (Mould et al. 1978).

Despite their short-timescale existence, FUors serve as crucial benchmarks in resolving the luminosity problem, and determining the final stellar mass of a given star. A FUor's disk makes for an important observation target, as a variety of accretion-mechanism models are focused on events occurring within the disk (Audard et al. 2014). A FUor's outflows also serve as an important target, as they can perturb and interact with an object's stellar envelope, thus possibly impacting its final mass. This project specifically focuses on HBC 494's wide-angle outflows, as they can provide information about the object's large-scale accretion mechanism, as well as their interactions with the stellar envelope and thus HBC 494's final mass.

.

1.3 HBC 494

The object of interest for this research, HBC 494, is a binary FUor type YSO embedded within the Orion A cloud and associated with reflection nebulae Re50N and Re50 (Ruíz-Rodríguez et al. (2017) and references therein). At 414 ± 7 parsecs from Earth, HBC 494 has a lower limit on its angular size of approximately 2.5 – 3″, which equates to a physical size of ∼1140 astronomical units; Ruíz-Rodríguez et al. (2017) also found an initial extension of ∼3″. Because of its binarity, HBC 494 presents a unique case for constraining FUor accretion outburst mechanisms. Due to the limitations of the standard thermal instability model (Audard et al. 2014), multiple solutions have been proposed in order to identify accretion outburst mechanisms among FUor type objects. The absence of well constrained binary FUor systems makes investigating externally triggered outbursts difficult, and at the same time makes HBC 494 a possible standard for binary (and higher order) YSO systems. Instabilities introduced into the circumbinary disk of a system such as HBC 494 may introduce similar instabilities into the individual protostellar disks, and thus trigger similar accretion outbursts from both protostars (Audard et al. 2014). While the binarity of a system may not be the sole cause for accretion outbursts, it can influence other high-magnitude events within the system.

Class I YSO's typically have opening outflow angles between 80 and 120° (Principe et al. 2017), however, HBC 494's northern outflow presents an opening angle of ∼150° (Ruíz-Rodríguez et al. 2017) (Sec. 3.2). These uncharacteristic outflows could result from the binarity of HBC 494, and may also be an indicator of poorly constrained/monitored accretion outburst mechanism.

Initial observations of HBC 494 taken in 2017 were limited in field of view and sensitivity due to the fact that only the ALMA main array was used. These limitations created an accuracy barrier on the physical and kinematic parameters of HBC 494, and thus the values produced by Ruíz-Rodríguez et al. (2017) are lower limits or underestimated. By re-observing HBC 494 with a combination of the ALMA 12m, ACA, and total power arrays, improvements in overall field of view, resolution, and sensitivity were made. The new observations of HBC 494 show a much larger extension of the objects

central outflows, which allows for a more accurate estimation of their physical and kinematic properties.

2 OBSERVATIONS AND DATA REDUCTION

A number of different emission lines were analyzed in order to determine various structural and chemical properties of HBC 494. The central protostar, located at $05^h\ 40^m\ 27.45024^s\ \ -07^\circ\ 27'\ 30.0564''$, and its surrounding emission were observed with the ALMA 12m main array, as well as a combination of the 12m, ACA, and total power arrays which will be called the 'combination array' for the remainder of this report. Observations were performed on three individual days in 2018: July 1st, July 12th, and July 13th. The July 1st observations spanned from 17:09:03.3 - 17:19:08.6 UTC, the July 12th observations spanned from 15:36:04.2 - 15:45:56.2 UTC, and the July 13th observations spanned from 12:44:40.0 - 12:54:31.3 UTC. With resolutions between 0.2 and 0.4″, the observations used for this project were able to resolve structure both large and small, including HBC 494's outflows, disk, and envelope.

The visibility data from the observations was edited, deconvolved, and viewed using CASA v6.2.0 (McMullin et al. 2007). The *tclean* function was used to deconvolve all observations, and the input parameters for this algorithm can be found in appendix B (Table B1).

3 DATA ANALYSIS

3.1 Gas emission lines

Emission lines with frequencies between 217 and 230 GHz were used to trace several spatial features of HBC 494, including outflows and their cavities, the stellar formation envelope, and various other emission regions (Table 2). Specifically, ^{12}CO, ^{13}CO, C^{18}O, SO, and DCN were observed between -5 and 18 km s^{-1}, with channels produced every 0.18 km s^{-1}. A doubly-peaked ^{12}CO line centered at 4 km s^{-1} implies a systemic velocity of the same value, which matches with Ruíz-Rodríguez et al. (2017)'s calculation. This observation is reinforced by significant ^{13}CO envelope emission (Fig. 4), as well as C^{18}O emission, as it typically traces lower kinematic motion. The system velocity can be difficult to constrain, however, as ^{12}CO and ^{13}CO trace different regions of HBC 494 with a mix of velocities and physical behaviors.

In terms of line-by-line results, ^{12}CO traces various cavities of HBC 494's high-energy outflows and helps to define a possible axis of rotation for the system (Ruíz-Rodríguez et al. 2017). ^{13}CO highlights the massive stellar envelope surrounding the central objects, as well as tracing interactions between the envelope and HBC 494's outflows. It also shows how outflows can impact the shape and overall structure of a stellar envelope. At redshifted velocities, C^{18}O traces regions similar to those highlighted by ^{13}CO emission, meaning that spatial coincidence between the two lines can indicate layered and complex structure. In the case of HBC 494, C^{18}O also traces material found in the disk. SO also traces disk material, as well as more dispersed material emitting form the secondary cavity.

3.2 Emission from ^{12}CO

^{12}CO emission is optically thick, which limits its use as a tracer for column density. However, ^{12}CO is able to trace material of ∼ 17K, making it the perfect line to observe HBC 494's wide-angle outflows and their cavities (Ruíz-Rodríguez et al. 2017). At blueshifted frequencies, main array observations show a downwards-facing curvature spatially coincident with continuum emission, indicating the presence of an outflow cavity. Although not as pronounced, combination array observations also detect this coincidence (Fig. 5).

Table 2. Each emission line used for observation, as well as their respective frequencies and general tracing uses.

Line	Frequency	Tracing use
^{12}CO	230.53800 GHz	Outflow cavities
^{13}CO	220.39869 GHz	Stellar envelope
SO	219.94944 GHz	Central object & outflow edges
C^{18}O	219.56035 GHz	Low density envelope regions
DCN	217.23853 GHz	No significant detection

In specific, the main array observations primarily map the upwards-facing curvature of the northern outflow, which indicates a bowl-like shape much similar to the blueshifted southern outflow. Combination array observations detail the outflow's general shape and opening angle, which is determined to be ∼ 150° (Ruíz-Rodríguez et al. 2017), and thus indicates a latitudinal size of approximately 30" (∼ 12400 au). In the redshifted velocity range at which the northern outflow is detected (5.08-9.4 km s^{-1}), notable ^{12}CO emission stemming from HBC 494's central protostar can be seen in main array observations. This emission elongates latitudinally as radio velocity approaches 5.8 km s^{-1}, and retracts again as the outflow detection begins to dissipate at 7.42 km s^{-1}, a phenomenon which possibly reinforces the bowl-like shape of the northern outflow. When emission between -5 and 16.96 km s^{-1} is combined into a moment 0 map, both of HBC 494's primary outflow cavities are well-defined and spatially coincident with previously reported observations at centered at ∼230 GHz (Ruíz-Rodríguez et al. 2017) (Fig. 6). Along with this emission, and for the first time ever, significant and well-defined upwards-facing curvature can be seen approximately 15″ north of HBC 494's continuum. Based on its position, intensity, size, and the velocities at which it was detected at, we believe that this secondary cavity originated from a previous large-scale accretion outburst. By studying this secondary cavity, we hope to determine when HBC 494's most recent outburst took place, and thus further constrain its large-scale accretion mechanism.

3.3 Emission from ^{13}CO

In the case of HBC 494, ^{13}CO is an optically thick line, although in certain regions it can be optically thin. The ^{13}CO line is useful for tracing large envelope-related features, and helps determine to what degree HBC 494 is embedded in its own star forming gas. It is also useful for tracing interactions between HBC 494's outflow cavities and its stellar envelope. The most significant and intense ^{13}CO emission from combination array observations begins at a blueshifted velocity of 3.1 km s^{-1} and persists up to a redshifted velocity of 6.16 km s^{-1}. Around systemic velocities (± 0.72 km s^{-1}), ^{13}CO traces HBC 494's massive stellar envelope, which covers other significant features detected with ^{12}CO, C^{18}O, and SO (Fig. C1). At its most prominent, the combination array emission stretches ∼ 60″ latitudinally and ∼ 70″ longitudinally, equating to an approximate area of $7.2 * 10^8$ au^2. However, due to the position of HBC 494 in the Orion A cloud, these ^{13}CO detections most closely represent a lower bound on the size of the stellar envelope as opposed to a final value. The combination array also detects prominent emission on the southern side of HBC 494 at blueshifted velocities, some of which appears to contour the curvature seen in ^{12}CO observations, which implies a possible connection between the envelope and southern

Figure 4. Emission intensity readings from ^{12}CO, ^{13}CO, C^{18}O, and SO from the 12m and combination ALMA arrays.

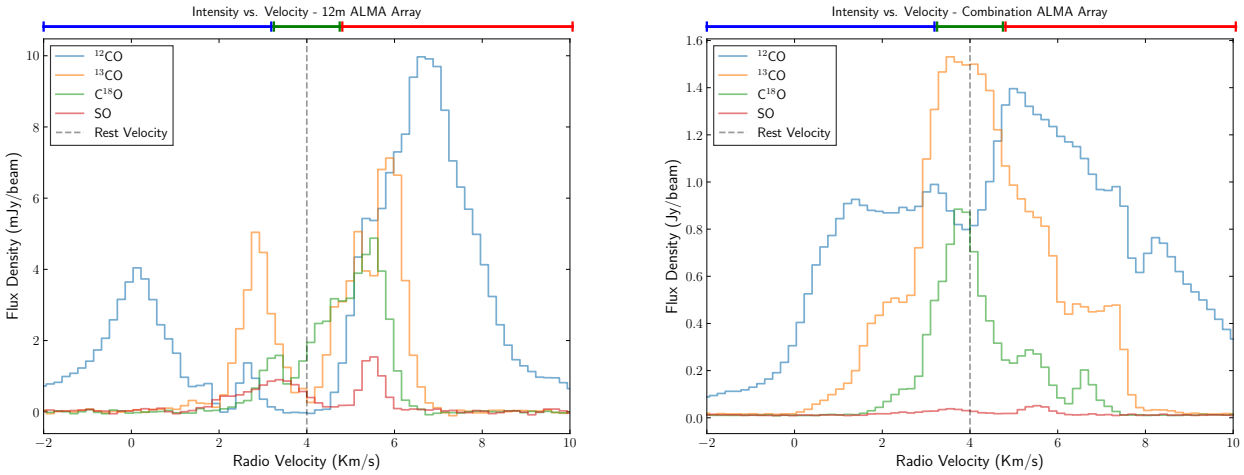

outflow. When viewed between radio velocities of 4.54 and 6.16 km s^{-1}, combination array ^{13}CO emission begins to trace HBC 494's secondary northern outflow, and becomes spatially coincident with ^{12}CO emission. However, the secondary outflow cavity appears to be much wider and maintains a greater ΔDec of approximately 20$''$ when viewed with ^{13}CO as opposed to the 15$''$ ΔDec of ^{12}CO. The difference between ^{12}CO and ^{13}CO observations is most likely due to the fact that the two lines may trace different layers of the upper cavity. This difference in both extension and position is aligned with Ruíz-Rodríguez et al. (2017)'s measurements of HBC 494's opening outflow angles, and further evidences the origin of the secondary northern cavity (Fig. 7). Main array observations at highly redshifted velocities also trace more nuanced features in the northern outflow, and possibly indicate how the stellar envelope can be repositioned by high-energy wide-angle outflows.

Overall, ^{13}CO provides more evidence which supports the origin of the secondary northern outflow cavity, as well as tracing the general structure of HBC 494's stellar envelope.

3.4 Emission from C^{18}O

In a similar fashion to ^{13}CO, C^{18}O is an optically thin line, which allowed it to be used as a tracer for the stellar envelope and various large-scale outflow features. In the case of HBC 494, C^{18}O was also used to trace material commonly found in the circumstellar disk. Combination array observations near systemic velocities reveal a strong coincidence with ^{13}CO envelope detections, which further reinforces the lower area limit on the envelope. Redshifted observations also show a large amount of material along the rim of the northern outflow, which appears to shift from east to west as velocity increases from 5.08 km s^{-1} to 5.95 km s^{-1} (Fig. C3). Despite their lower overall intensity, redshifted main array observations also show a 'wave' of material travelling outwards from the center of the northern ^{12}CO curvature (Fig. C4). When combined into moment 0 and moment 1 maps, this 'wave' of emission maintains both similar shape and position to the ^{12}CO and ^{13}CO observations of HBC 494's secondary northern cavity (Fig. 8). At blueshifted velocities, the main array captures emission in a similar shape to the southern curvatures observed with ^{12}CO, although at a much lower intensity.

3.5 Emission from SO

The optical density of SO can be impacted by multiple factors such as gas density, pressure, and temperature. In the case of HBC 494, SO is an optically thick line, making it useful for observing small-scale structure around the object's disk and monitoring the binarity of the system. SO also responds to 'shocked' outflow regions, some of which are visible in both combination and main array observations. Both main and combination array observations at redshifted velocities show SO spatially consistent with both ^{12}CO and C^{18}O detections, implying that a connection may exist between excited SO and gas-rich regions of stellar outflows. Starting at 1.48 km s^{-1}, main array observations show a lobe of relatively low-intensity emission forming to the west of HBC 494's disk, which may represent either a binary companion or a formation event enclosed within the disk. The lobe splits into two parts, one to the west and one to the south, near systemic velocities and begins to retract at redshifted velocities (Fig. C2). In relation to the previously mentioned secondary outflow curvature, SO is able to trace minimal amounts of structure in comparison to ^{12}CO, ^{13}CO, and C^{18}O. However, SO is able to trace northeastern regions of the cavity, whereas other emission lines are not (Fig. 9).

3.6 Emission from DCN

Unlike the four previously discussed observations, DCN traced nothing but noise, indicating a non-detection at the observed resolution and sensitivity. DCN was meant to trace possible high-energy (UV, X-ray) emission stemming from HBC 494's central objects. While not as useful as a detection, the DCN results can still reveal some important information. At 400 L$_\odot$, HBC 494 is a relatively bright FUor, meaning that DCN observations could have been obfuscated and thus show a non-detection. It is possible that an error propagated throughout the cleaning process. However, the four previously discussed emission lines were cleaned with the same procedure and came from the same observing campaign as DCN, meaning that the likelihood of these errors occurring is slim. In the future, DCN will be re-observed in hopes of getting better and more conclusive results.

Figure 5. Moment 0 maps of blueshifted 12m (top) and combination (bottom) array ^{12}CO emission. HBC 494's central southern outflow is primarily traced by this emission. [BMAJ = 4.363546848400∗10^{-4} deg, BMIN = 3.056263872971∗10^{-4} deg, RMS = 5.2∗10^{-1} Jy/beam.km/s, Velocity range = -2.3 - 0.76 & 7.42 - 11.02 km s^{-1}]

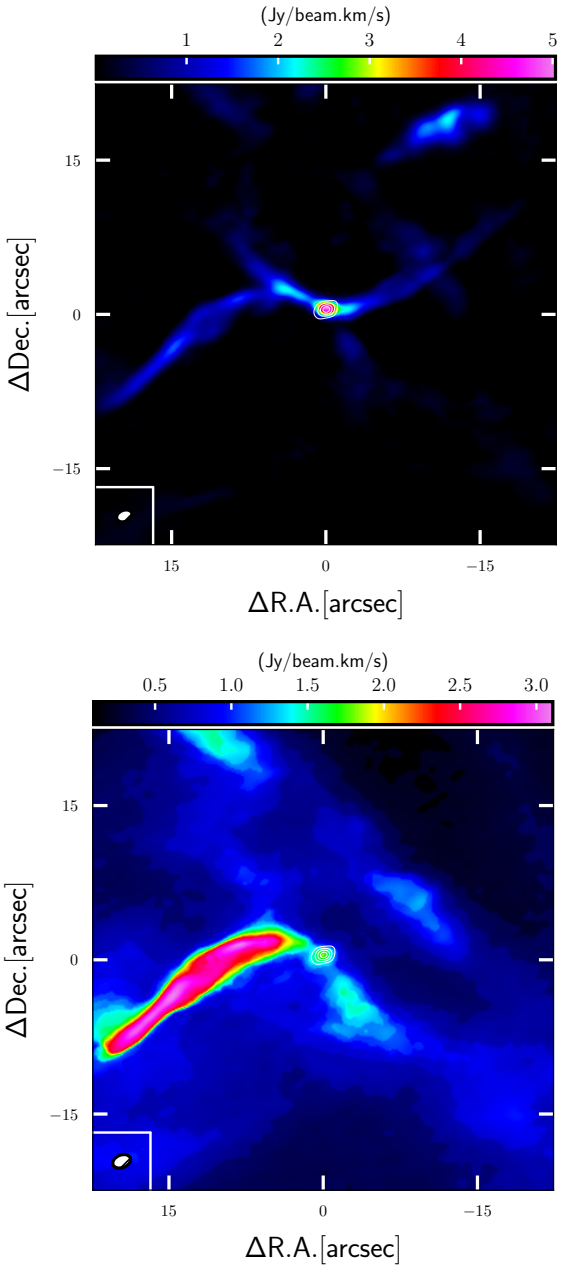

Figure 6. A moment 0 map of HBC 494's primary and secondary outflow cavities as observed with ^{12}CO. [BMAJ = 4.363546848400∗10^{-4} deg, BMIN = 3.056263872971∗10^{-4} deg, RMS = 6.8∗10^{-1} Jy/beam.km/s, Velocity range = -5 - 16.96 km s^{-1}]

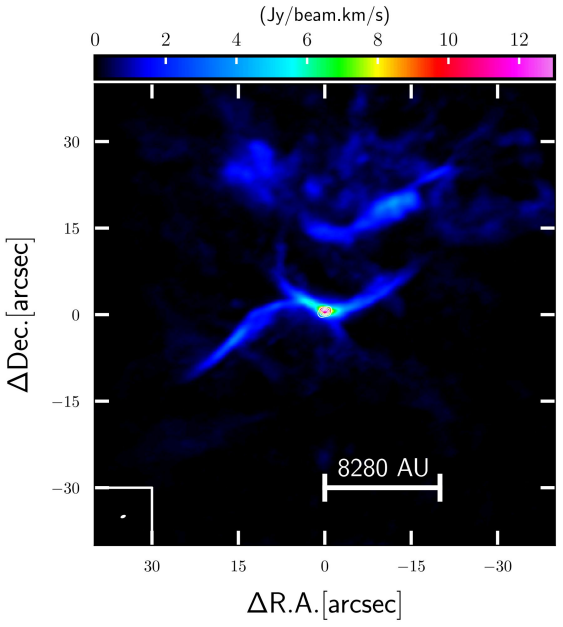

Figure 7. A moment 0 map of HBC 494's primary and secondary outflow cavities as observed with ^{13}CO. [BMAJ = 4.363546848400∗10^{-4} deg, BMIN = 3.056263872971∗10^{-4} deg, RMS = 1.9∗10^{-1} Jy/beam.km/s, Velocity range = 4.54 - 6.16 km s^{-1}]

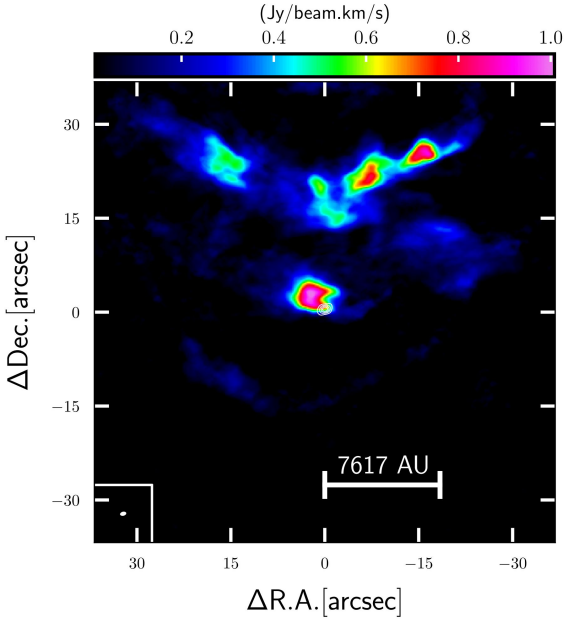

4 DISCUSSION

While previous studies of HBC 494 have revealed important information about the object's structure, mechanisms, and location on the evolutionary timeline, this research in combination with previous preliminary results has provided *nearly* full picture of HBC 494. The discussion section will primarily focus on how the results from this research compare with those from previous publications, and what steps can be taken in the future to further our studies of HBC 494.

4.1 Wide-angle outflows

The most prevalent difference between previous observations of HBC 494 (2017) and those used in this project (2018) is field of view. 2017 observations cover an area of approximately 64 arcseconds^2, while 2018 observations cover a much larger area of about 1600 arcseconds^2, a factor of 25 times greater. Due to their limited nature,

Figure 8. Moment 0 (left) and moment 1 (right) maps of $C^{18}O$ emission. Both of these maps trace notable bipolar outflows. [BMAJ = $4.363546848400*10^{-4}$ deg, BMIN = $3.056263872971*10^{-4}$ deg, RMS = $9.2*10^{-2}$ Jy/beam.km/s (moment 0), RMS = 4.6 km/s (moment 1), Velocity range = 2.74 - 6.16 km s^{-1}]

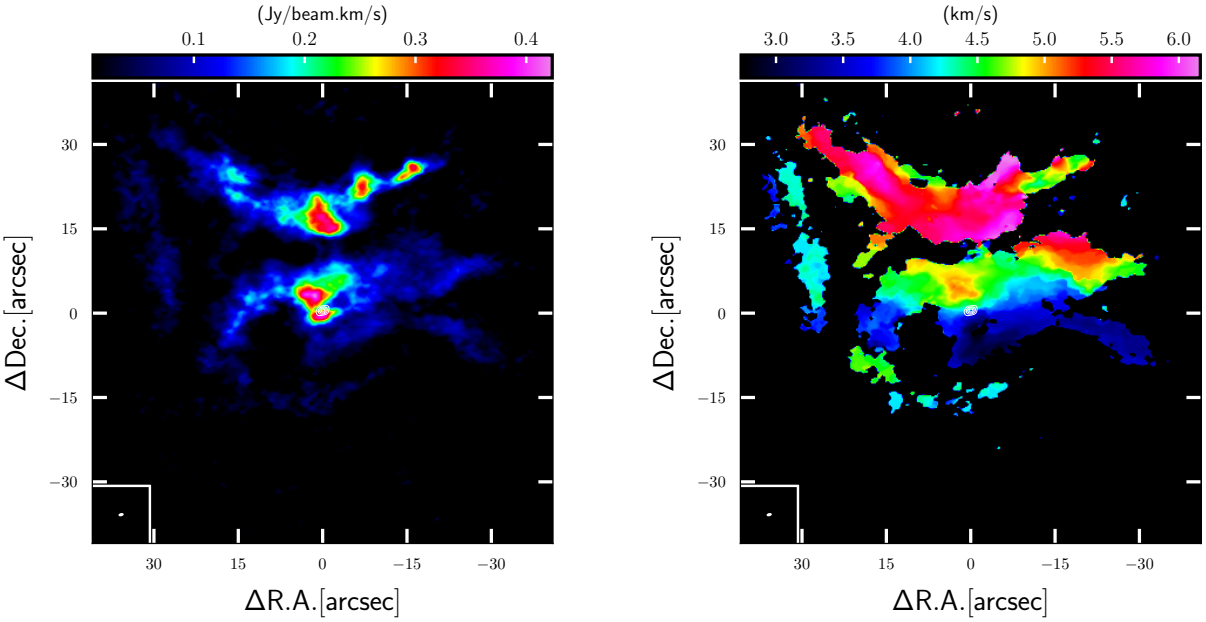

Figure 9. A moment 0 map of HBC 494's secondary outflow cavity as traced with SO. [BMAJ = $4.363546848400*10^{-4}$ deg, BMIN = $3.056263872971*10^{-4}$ deg, RMS = $2.5*10^{-2}$ Jy/beam.km/s, Velocity range = 5.08 - 6.16 km s^{-1}]

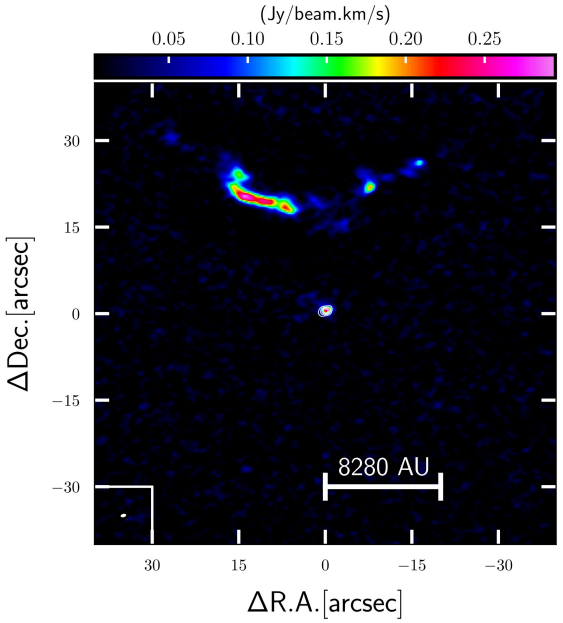

the 2017 observations show that HBC 494's central outflows span about 16 arcseconds horizontally and 5 arcseconds vertically, which corresponds to a true size of approximately 6600 AU horizontally and 2070 AU vertically (Fig. 10). In comparison, the 2018 observations show a horizontal extension of approximately 45 arcseconds horizontally and 25 arcseconds vertically, which corresponds to a size of about 18,600 AU horizontally and 10,300 AU vertically. This change in overall extension allows for more accurate and more precise calculation of the central outflow's kinematic properties, which in turn provides more insight into HBC 494's primary accretion mechanism.

The field of view improvements made by the 2018 observations can also aid in resolving the discrepancy between HBC 494's primary classification and outflow opening angle (Principe et al. 2017). ^{13}CO and $C^{18}O$ observations from 2018 show a substantial amount of material surrounding HBC 494's central objects at both blueshifted and redshifted velocities, areas which were not present in the 2017 observations. This emission appears to 'fill in' the curvature detected with ^{12}CO, which helps to gain a full picture of the central outflow's structure. Because $C^{18}O$ typically traces material found in the circumstellar disk, these detections indicate that there exists a considerable interaction between HBC 494's disk and its outflows, and thus a similar interaction could exists between the object's accretion mechanism and its outflows.

Ruíz-Rodríguez et al. (2017) suggests that high energy outflows, such as HBC 494's, should decrease the mass of individual stars in a stellar neighborhood, but increase the number of objects within the group itself. If future observations show signs of possible star formation close to HBC 494, the impact of the object's outflows could be understood even more.

4.2 The secondary cavity

Arguably the most important result this project produced was the discovery of the secondary northern outflow. While intermediate observations of the predicted accretion outburst do not exist, primarily for the reasons discussed in the previous section, the secondary cavity as it is recorded in the observations used for this research can still provide a great amount of information about HBC 494. Primarily, this cavity can be used to to help estimate the properties of an unrecorded outburst (Audard et al. 2014). Constraining the timing of this outburst is helpful in determining other factors concerning HBC 494, such as accretion changes, kinematics, and outflow extension, all of which can impact the evolution of the object's disk. These

Figure 10. ^{12}CO observations of HBC 494 from the 2017 observation campaign (Ruíz-Rodríguez et al. 2017)

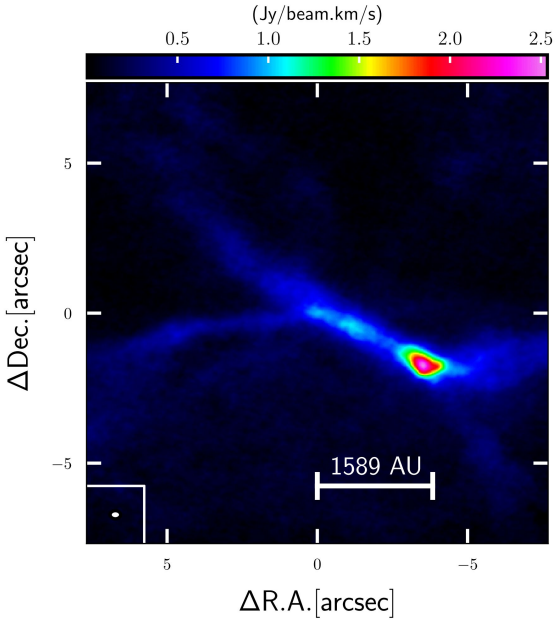

Table 3. A table showing all the yet-to-be observed lines, their frequencies, and transitions.

Line	Frequency	Transition
SiO	217.105 GHz	$5 \rightarrow 4$
DCN	217.238 GHz	$J = 3 \rightarrow 2$
H_2CO	218.790 GHz	$3_{2,2} \rightarrow 2_{2,0}$
SO_3	219.949 GHz	$6_5 \rightarrow 5_4$
^{13}CS	231.221 GHz	$5 \rightarrow 4$
CH_3OH	251.861 GHz	$4_3^- \rightarrow 4_2^+$
HCN	265.886 GHz	$J = 3 \rightarrow 2$
HCO^+	267.558 GHz	$J = 3 \rightarrow 2$

factors can also provide into HBC 494's binarity and the magnitude at which it impacts the system's accretion outburst mechanism.

4.3 Future work

There is much more work to be done on this project, most of which will be observing and analyzing more emission lines. Table 3 displays all of the lines we plan to observe, as well as their frequencies and corresponding rotational transitions. While ^{12}CO, ^{13}CO, C^{18}O, and SO provided useful information about HBC 494's structure and other properties, we hope that these new lines will lead to even more discoveries.

The next two main goals for this project are as follows: determine the magnitude at which the binarity of HBC 494 impacts its outburst mechanics, and estimate the kinematic properties of the secondary northern outflow cavity.

5 CONCLUSIONS

ACKNOWLEDGEMENTS

First and foremost, I want to thank Dary Ruíz. This project would not even have taken place if it weren't for her, and I'm incredibly thankful for the opportunity to have done research at the NRAO. I also want to thank Dr. Jim Braatz, Dr. Will Armentrout, and Dr. Anna Kapinska for hosting the many site meetings that took place every week and for hosting the final symposium at the Green Bank Observatory. Finally, I want to thank my parents for inspiring me to commit myself to science. Even though it's about six years away, I really want to be the third Dr. Fourkas in the family.

REFERENCES

Arce H. G., Borkin M. A., Goodman A. A., Pineda J. E., Halle M. W., 2010, The Astrophysical Journal, 715, 1170
Audard M., et al., 2014, Protostars and Planets VI
Kenyon S. J., Kolotilov E. A., Ibragimov M. A., Mattei J. A., 2000, The Astrophysical Journal, 531, 1028
McMullin J. P., Waters B., Schiebel D., Young W., Golap K., 2007, in Shaw R. A., Hill F., Bell D. J., eds, Astronomical Society of the Pacific Conference Series Vol. 376, Astronomical Data Analysis Software and Systems XVI. p. 127
Mould J. R., Hall D. N. B., Ridgway S. T., Hintzen P., Aaronson M., 1978, ApJ, 222, L123
Principe D. A., et al., 2017, Monthly Notices of the Royal Astronomical Society, 473, 879–895
Ruíz-Rodríguez D., et al., 2017, Monthly Notices of the Royal Astronomical Society, 466, 3519–3532
Siwak M., et al., 2013, Monthly Notices of the Royal Astronomical Society, 432, 194
Williams J. P., Cieza L. A., 2011, Annual Review of Astronomy and Astrophysics, 49, 67–117

APPENDIX A: EXTRA SUMMER ACTIVITIES/EVENTS

Aside from conducting this research, I took part in a multitude of different activities and groups this past summer, the prominent of which was the Summer Student Star Formation Group (S^{3}FG). This group was composed of 12 members, six from the NRAO Summer REU program, and six from the UVA-CASSUM CICOVICO Summer REU. This group focused on multiple aspects of being an astronomer, from reading and understanding research papers, to presenting our own research, to promoting ourselves as up-and-coming scientists. I also participated in the NRAO-organized PGRE workshop. I learned that although the PGRE seems to be a flawed intelligence benchmark, it shows that physics isn't necessarily all number crunching and formula memorization. Physics leaves room for ingenuity and wit

APPENDIX B: CODING / CASA

This section lists any coding packages, parameters, or scripts that were usedful in processing our data and making images. Python was the only language used, and CASA was the primary data processing tool.

APPENDIX C: FIGURES

This paper has been typeset from a TEX/LATEX file prepared by the author.

Figure C1. HBC 494's stellar envelope as observed with ^{13}CO through the ALMA combination array.

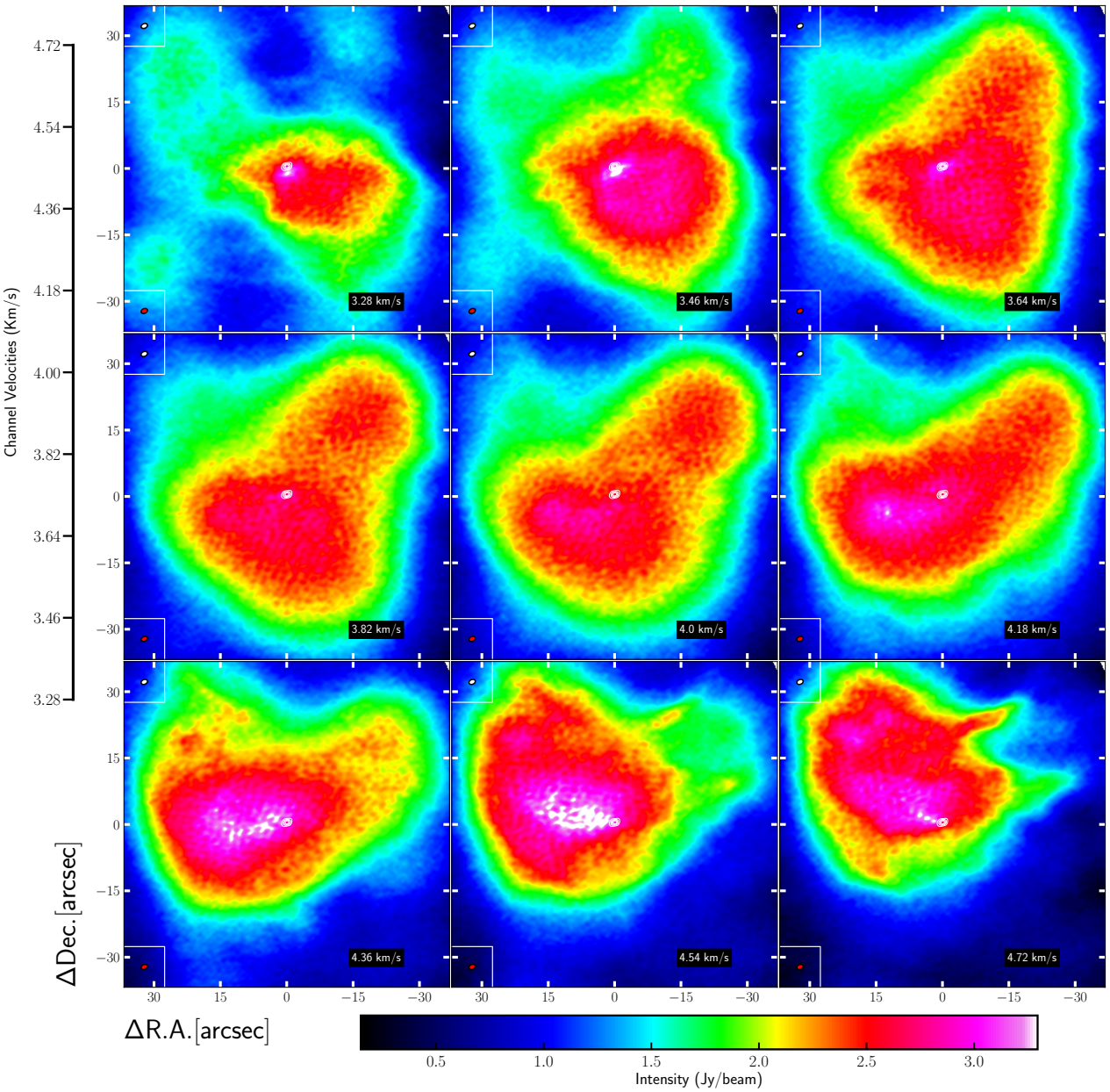

Figure C2. Main array detections of SO near the HBC 494's disk.

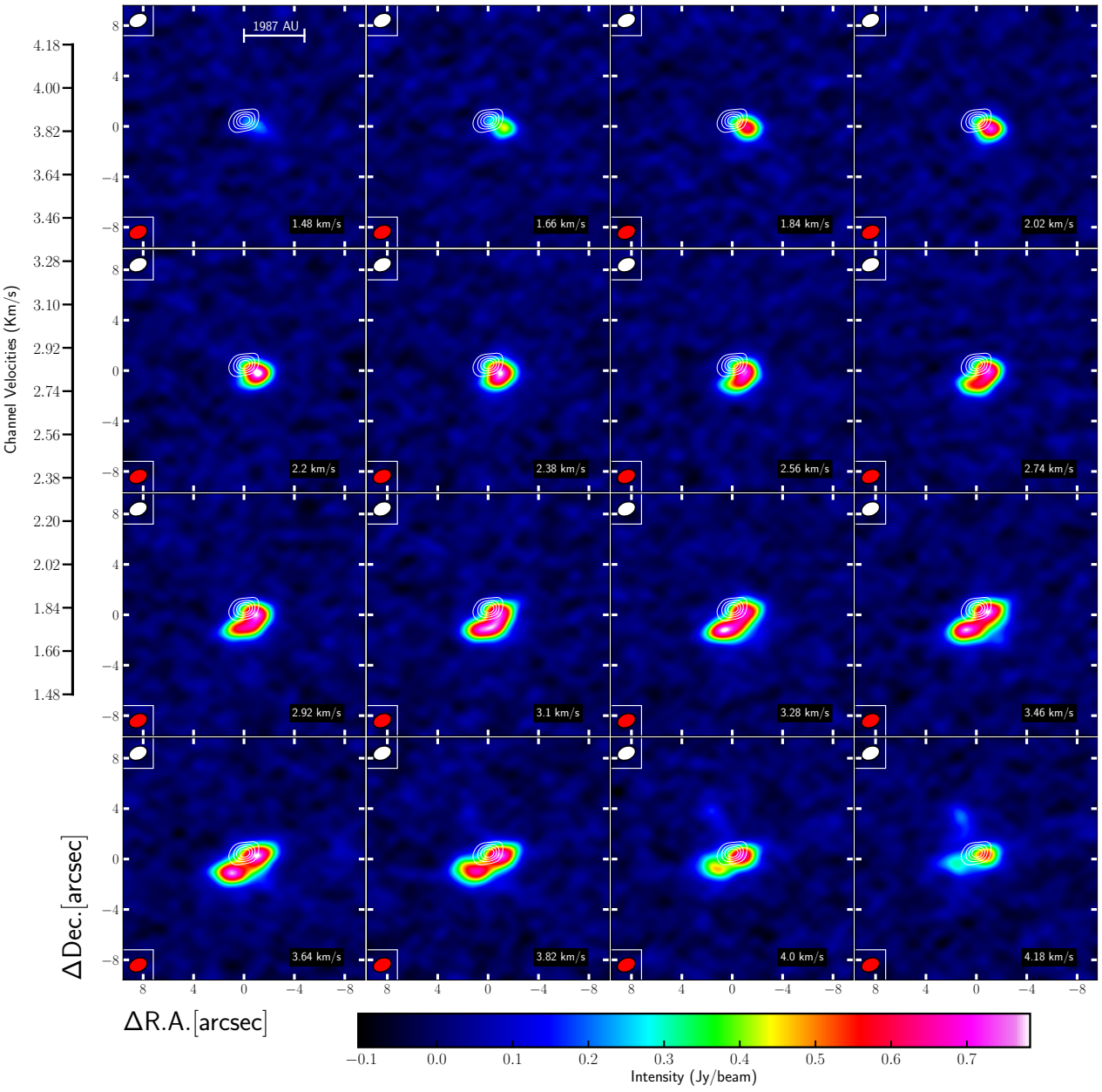

Figure C3. Channel maps of the northern outflow detections with $C^{18}O$ through the combination array.

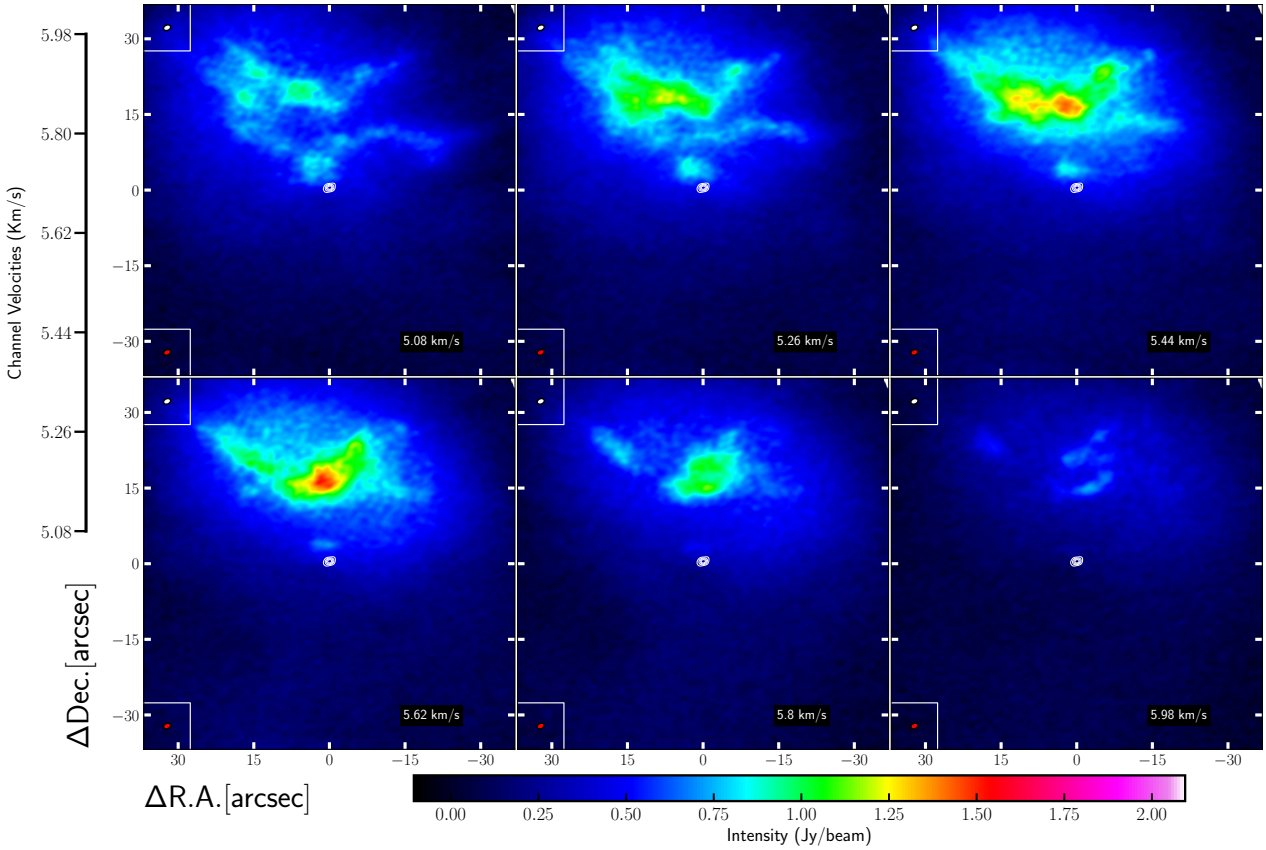

Figure C4. Channel maps of the northern outflow detections with $C^{18}O$ through the main array.

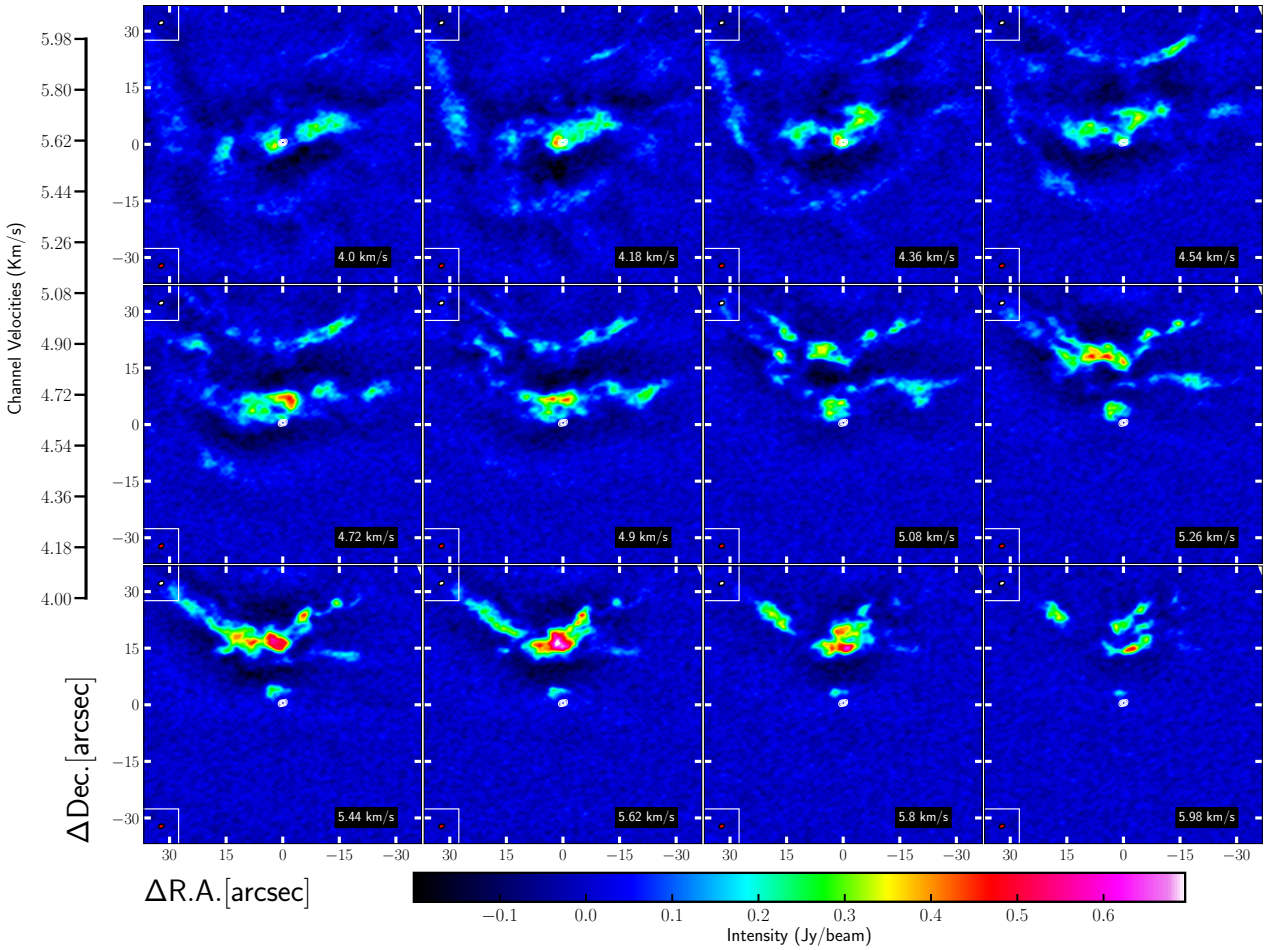

Table B1. All parameters used for CASA's tclean function. Values in parenthesis are presented as plain-text and are not to be taken literally

Parameter	Value
field	(blank)
spw	(blank)
pbmask	0
nchan	90
start	-5 Km/s
width	0.18 Km/s
veltype	radio
phasecenter	J2000 05h40m27.45024 -07d27m30.0564
restfreq	(Depends on line)
imsize	[512, 512]
cell	0.16arcsec
robust	0.5
niter	1000
deconvolver	hogbom
interactive	False
weighting	briggs
restoringbeam	common
outframe	LSRK
specmode	cube
gridder	mosaic

Table B2. All of the python packages used for this project and their specific purposes. Packages which are pre-installed with python are not listed

Package	Use
matplotlib	Processing final plots
numpy	Performing calculation
astropy	Importing data
scipy	Performing calculation
pandas	Reading CSV files
lmfit	Curve fitting
uncertainties	Determining uncertainties
spectralcube	Looping over FITS data